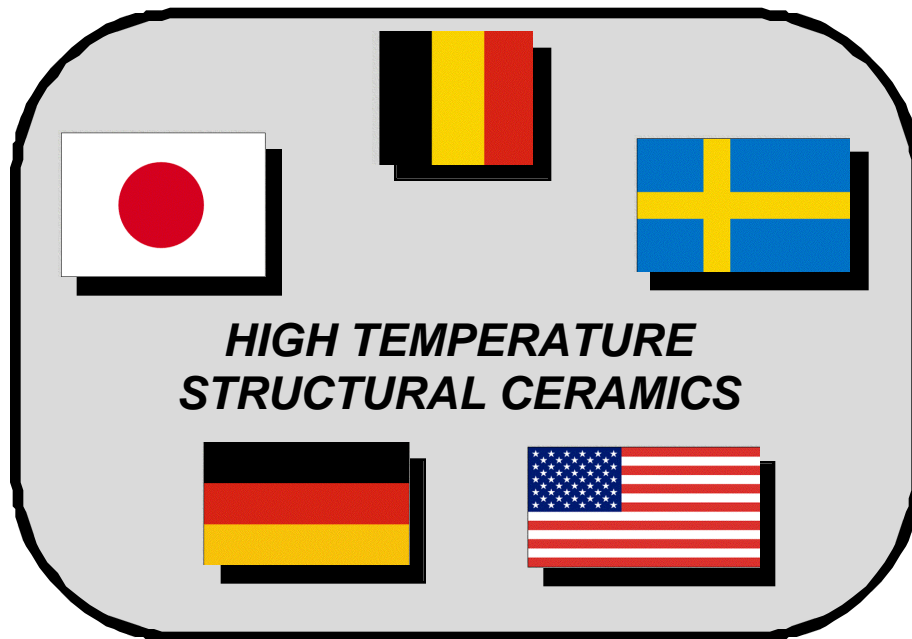


Thermal and Mechanical Fatigue Testing of Advanced Ceramics - Subtask 11

International Energy Agency Implementing Agreement
For A Programme Of Research And Development On
Advanced Materials For Transportation Applications



United States Report

June 2003

This document contains information whose distribution is governed by an International Energy Agency Implementing Agreement for a Co-operative Programme of Research and Development on High Temperature Materials for Automotive Engines and Other Conservation Applications (IEA Annex II), between Belgium, Germany, Japan, Sweden, and the United States. This Report shall not be disseminated to any parties other than the Participants in this Annex Agreement for a one-year period commencing from the publication date unless specifically agreed to by the Executive Committee of IEA Annex II. Following the one-year period, the information will be available for public release.

Research sponsored by the U.S. Department of Energy, Assistant Secretary for Energy Efficiency and Renewable Energy, Office of Transportation Technologies, as part of the Heavy Vehicle Propulsion System Materials Program, under contract DE-AC05-96OR22464 with UT-Battelle LLC.

INTRODUCTION

Background

The development of new and improved ceramic materials, design methods for brittle materials, and life prediction methodology is of vital importance to the successful utilization of structural ceramics in advanced heat engine applications for transportation applications. In order to address these issues on an international level, a cooperative research agreement was initiated by several countries under the International Energy Agency (IEA). The original effort was started in 1979 through an Implementing Agreement for a Program of R&D on High-Temperature Materials for Automotive Engines. This agreement was completed in FY 1985, with DOE serving as Operating Agent for the United States. In this first agreement entitled, "Annex I-Ceramics for Automotive Gas Turbine Engines," the United States and Germany conducted information exchange and experimental ceramic materials and test results on those materials via participation of industrial and government laboratories in both countries.

Annex II, the current IEA agreement under which this international research is conducted, was started in 1985. The current participants are Germany, United States, Sweden, Japan, and Belgium. The United States Department of Energy is the Chairman of the Executive Committee and Operating Agent for Annex II. The active subtasks are (1) Subtask 9 - Thermal Shock Testing of Advanced Ceramics and (2) Subtask 10 - Characterization of Ceramic Powders. The purpose of Subtask 9 is to assess advanced techniques for the measurement of thermal shock of silicon nitride and other structural ceramics. The objectives of Subtask 10 are to (1) tighten and finalize procedures for characterization of secondary properties of selected powders; (2) delineate interrelationships between primary and secondary properties; and (3) unify IEA efforts with those of ASTM, CEN, and JIS—leading to ISO adaptation.

This report summarizes the Subtask 11 research activities, which involved participation from Germany, Japan, and the United States. The primary objective of this effort was to develop and verify techniques for the measurement of thermal and mechanical fatigue of structural ceramics. National efforts in Japan and the United States focussed on the development of procedures for evaluating the mechanical fatigue behaviour of silicon nitride ceramics using either uniaxial flexure or biaxial test specimens. The national effort in Germany consisted of the development of thermal fatigue procedures using the laser thermal shock equipment evaluated in Subtask 9 [1].

Subtask 11 also included an international effort in which the thermal and mechanical fatigue behaviour of a single silicon nitride was compared with the mechanical fatigue data generated at a temperature which is the same as that at the fracture point in thermal fatigue test. Germany was responsible for the thermal fatigue testing while both Japan and the United States conducted mechanical fatigue testing.

This report describes the activities conducted within the United States. These activities included the measurement of static, dynamic, and cyclic fatigue properties of a commercial silicon nitride. The section that follows provides a mathematical treatment of the three types of behavior.

A Generalized Approach for Static, Dynamic, and Cyclic Fatigue

We start by assuming that for a given flaw size, a , the associated fracture strength, S , is given as,

$$Y S (a)^{1/2} = K_{IC} , \quad (1)$$

where Y is a constant and K_{IC} is the fracture toughness. More generally when the applied stress, σ , is less than the fracture strength, Equation 1 becomes

$$Y \sigma (a)^{1/2} = K_I, \quad (2)$$

where K_I is the stress intensity factor. When slow crack occurs the crack length increases in accordance with power law equation,

$$da/dt = V = A K_I^N, \quad (3)$$

where A and N are constants, V is the crack velocity, t is time, and K_I is the stress intensity factor. The K_I term in Equations 2 and 3 can be eliminating yielding the expression,

$$da/dt = V = A (Y \sigma (a)^{1/2})^N, \quad (4a)$$

or

$$da/(a)^{N/2} = A (Y \sigma)^N dt. \quad (4b)$$

After integrating each side one has that

$$[(a_f)^{-N/2+1} - (a_i)^{-N/2+1}] / (-N/2+1) = A Y^N \sigma^N dt \quad (5a)$$

or after rearrangement

$$[(a_i)^{-N/2+1} - (a_f)^{-N/2+1}] = (N - 2)/2 A Y^N \sigma^N dt, \quad (5b)$$

where a_i and a_f are the initial and final crack lengths, respectively. These crack lengths can be related to the fracture strengths as follows

$$Y S_i (a_i)^{1/2} = K_{IC}, \quad (6a)$$

and

$$Y S_f (a_f)^{1/2} = K_{IC}. \quad (6b)$$

where S_i is the inert strength and S_f is the strength after time, t . Consequently, Equation 5 can be rewritten as

$$[(Y S_i / K_{IC})^{N-2} - (Y S_f / K_{IC})^{N-2}] = (N - 2)/2 A Y^N \sigma^N dt \quad (7a)$$

or

$$[(S_i)^{N-2} - (S_f)^{N-2}] = (N - 2)/2 A (K_{IC})^{N-2} Y^2 \sigma^N dt. \quad (7b)$$

or

$$[1 - (S_f / S_i)^{N-2}] = (N - 2)/2 A (K_{IC})^N (K_{IC} / S_i)^{-2} Y^2 (\sigma / S_i)^N dt. \quad (7c)$$

or

$$[1 - (S_f/S_i)^{N-2}] = (N - 2)/2 V(K_{IC}) (Y S_i/K_{IC})^2 (\dot{S}_i)^N dt. \quad (7d)$$

or

$$[(S_i)^{N-2} - (S_f)^{N-2}] / [(S_o)^{N-2}] = (N - 2)/2 V(K_{IC}) (Y S_o/K_{IC})^2 (\dot{S}_o)^N dt. \quad (7e)$$

where we have used the fact that $V(K_{IC}) = A K_{IC}^N$.

If the stress is constant, the integral on the right hand side of Equation 7b is $\dot{S}_i^{-N} t$, yielding the following expression,

$$[(S_i)^{N-2} - (S_f)^{N-2}] = (N - 2)/2 A (K_{IC})^{N-2} Y^2 \dot{S}_i^{-N} t. \quad (8a)$$

or

$$[1 - (S_f/S_i)^{N-2}] = (N - 2)/2 V(K_{IC}) (Y S_i/K_{IC})^2 (\dot{S}_i)^N t. \quad (8b)$$

In this case failure occurs when $S_f = S_i$. For a constant stressing rate, $\dot{S}_i = (dS/dt) t$ and Equation 7b becomes:

or

$$[(S_i)^{N-2} - (S_f)^{N-2}] = [(N-2)/(2(N+1))] A Y^2 (K_{IC})^{N-2} (\dot{S}_i)^{N+1} t^{N+1}. \quad (9a)$$

or

$$[1 - (S_f/S_i)^{N-2}] = [(N-2)/(2(N+1))] V(K_{IC}) (Y S_i/K_{IC})^2 (\dot{S}_i)^{N+1} t^{N+1}. \quad (9b)$$

or

$$[1 - (S_f/S_i)^{N-2}] = [(N-2)/(2(N+1))] V(K_{IC}) (Y S_i/K_{IC})^2 (\dot{S}_i)^N t. \quad (9c)$$

or

$$[1 - (S_f/S_i)^{N-2}] = [1/(N+1)] [(N-2)/2] V(K_{IC}) (Y S_i/K_{IC})^2 (\dot{S}_i)^N t. \quad (9d)$$

For cyclic loading the applied stress is a periodic function of time ($S_i = S_{max} f(t)$) such that

$$(\dot{S}_i)^N dt = (S_{max}/S_i)^N (\dot{S}_i)^N [(1/\dot{S}_i) \int_0^{\dot{S}_i} f(t)^N dt] = (S_{max}/S_i)^N (\dot{S}_i)^N I_{cyc}. \quad (10)$$

where N_{cyc} is the number of cycles and I_{cyc} is the value of the integral represented in brackets. Note that we have integrated the expression over one cycle (with period \dot{S}_i). When $t \gg \dot{S}_i^{-1}$, N_{cyc} is approximated by the quantity t/\dot{S}_i^{-1} . The expression for time-dependent strength becomes

$$[1 - (S_f/S_i)^{N-2}] = (N - 2)/2 V(K_{IC}) (Y S_i/K_{IC})^2 (S_{max}/S_i)^N (N_{cyc}) I_{cyc}. \quad (11)$$

Note that for static loading $S_i = S_{max}$, $t = N_{cyc} \dot{S}_i^{-1}$, and $I_{cyc} = 1$ such that Equation 11 becomes identical to equation 8b.

EXPERIMENTAL PROCEDURE

Material and Specimen Geometries

GS44 silicon nitride (manufactured by Honeywell Ceramics Components) was used for all testing in the United States. This material is cold isostatically pressed (CIPed) and then gas pressure

sintered using 4 w/o Y_2O_3 and 4 w/o spinel ($MgAl_2O_4$) as densification aids. A typical microstructure of the as-fabricated material is shown in Figure 1. X-ray diffraction results for as-fabricated specimens showed only the presence of Si_3N_4 suggesting the intergranular phase was amorphous.

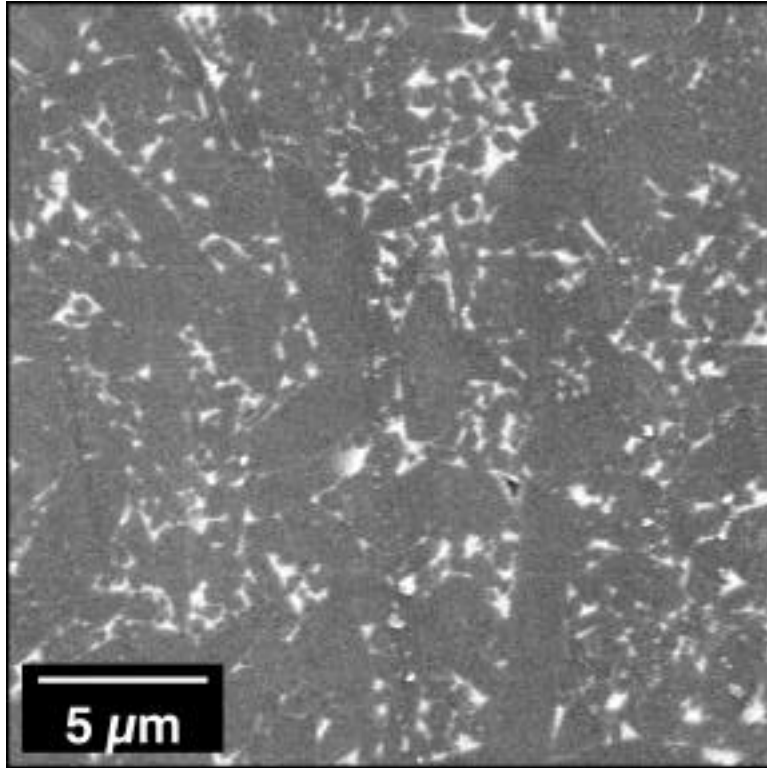
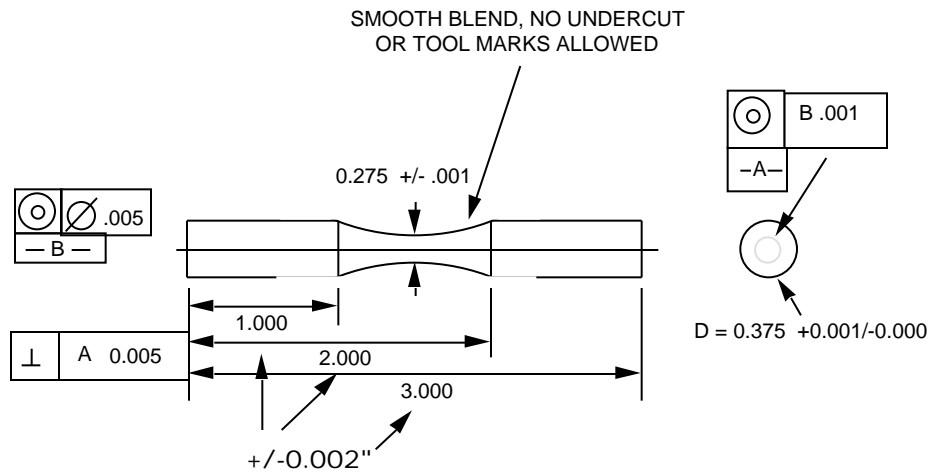


Figure 1: Typical microstructure of GS44 silicon nitride.

Two types of test specimens were machined from the as-received billets of the GS44. The first was Size B flexure bars with nominal dimensions of 3 by 4 by 50 mm. These specimens were used for both static and dynamic fatigue testing (described below). The second specimen type was a cylindrical dog-bone specimen (Figure 2) used for the rotary bend fatigue (RBF) tests.

Test Equipment and Conditions

The static and dynamic fatigue tests were conducted the Flexure Test System (FTS), which provides for the application of selected load-time profiles to flexure, compression, c-ring, and o-ring specimens at elevated temperatures (Figure 3). A maximum of three specimens can be simultaneously tested at temperatures up to 1600°C. The loads are generated by pneumatically-driven air cylinders located at the top of the support frame. In order to minimize impact problems normally encountered during fracture, a hydraulic fluid is used as the working medium in the cylinder. The cylinder pressure and thus, the applied load is controlled by an I/P transducer. The mechanical loads are transmitted into the hot zone of the furnace through SiC rods. Each of the bottom three SiC support rods is also attached to a load cell which monitors the applied force. Load-point displacement for each load train is determined by an SLVC, which is attached to the upper load rod. Finally, the temperature is monitored with a Type S thermocouple attached to the middle load rod.



- SURFACE FINISH $0.4 \mu\text{m}$ ALL OVER
- FINAL GRIND OF GAGE SECTION TO BE TRANSVERSELY MACHINED
- MATERIAL: 95 % Al_2O_3 (SUPPLIED)
- ALL DIMENSIONS IN INCHES
- NOTE: RUNOUT CAN NOT EXCEED .002"

Figure 2: Rotary bend fatigue specimen.

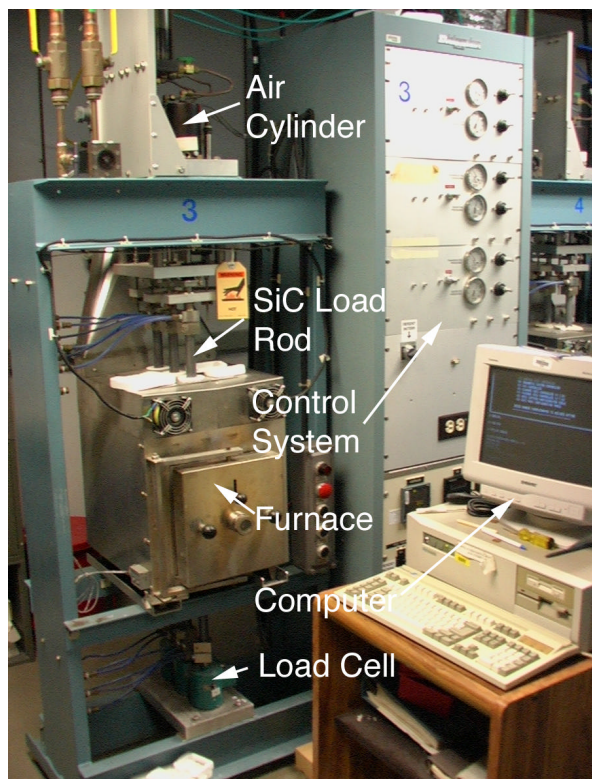


Figure 3: Key components of Flexure Tests System.

A data acquisition system (DAS) is used to digitize the load cell, SLVC, and thermocouple signals as well as monitor various FTS status signals including furnace door interlock, water flow indicator, and fracture detection. In addition, the DAS provides three 4 to 20 MA outputs required to control the I/P transducers. The status of four solid state relays is also controlled by the DAS. Three of these relays are used to open and close solenoid valves located between the air cylinder and I/P transducer. The fourth solid state relay energizes the furnace relay, which provides power to the furnace elements.

For the current program static and dynamic fatigue tests were conducted at 850°C. For static fatigue testing, the applied stresses ranged from 400 to 750 MPa. Two stressing rates, 30 and 0.003 MPa/s, were used for the dynamic fatigue tests. Additional details are provided in Ref [2].

The initial configuration of the rotary bend fatigue (RBF) machine being used for this effort is shown in Figure 4 while Figure 5 illustrates the loading configuration. Note that the dead weight loading that is normally used to generate stresses in the specimens was replaced by a computer controlled pneumatic loading system. This system could either maintain a static load or control the load as a function of time.

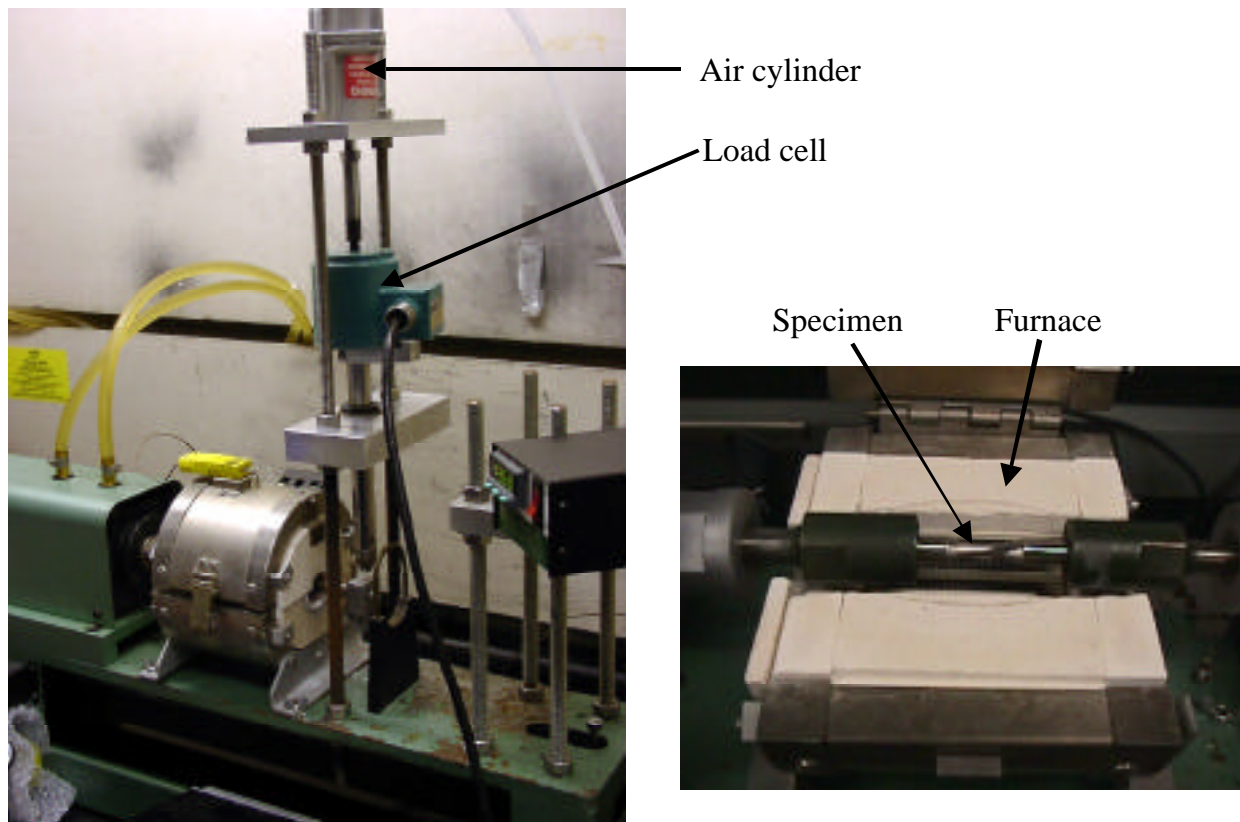


Figure 4: Rotary fatigue machine modified with computer-controlled pneumatic loading system.

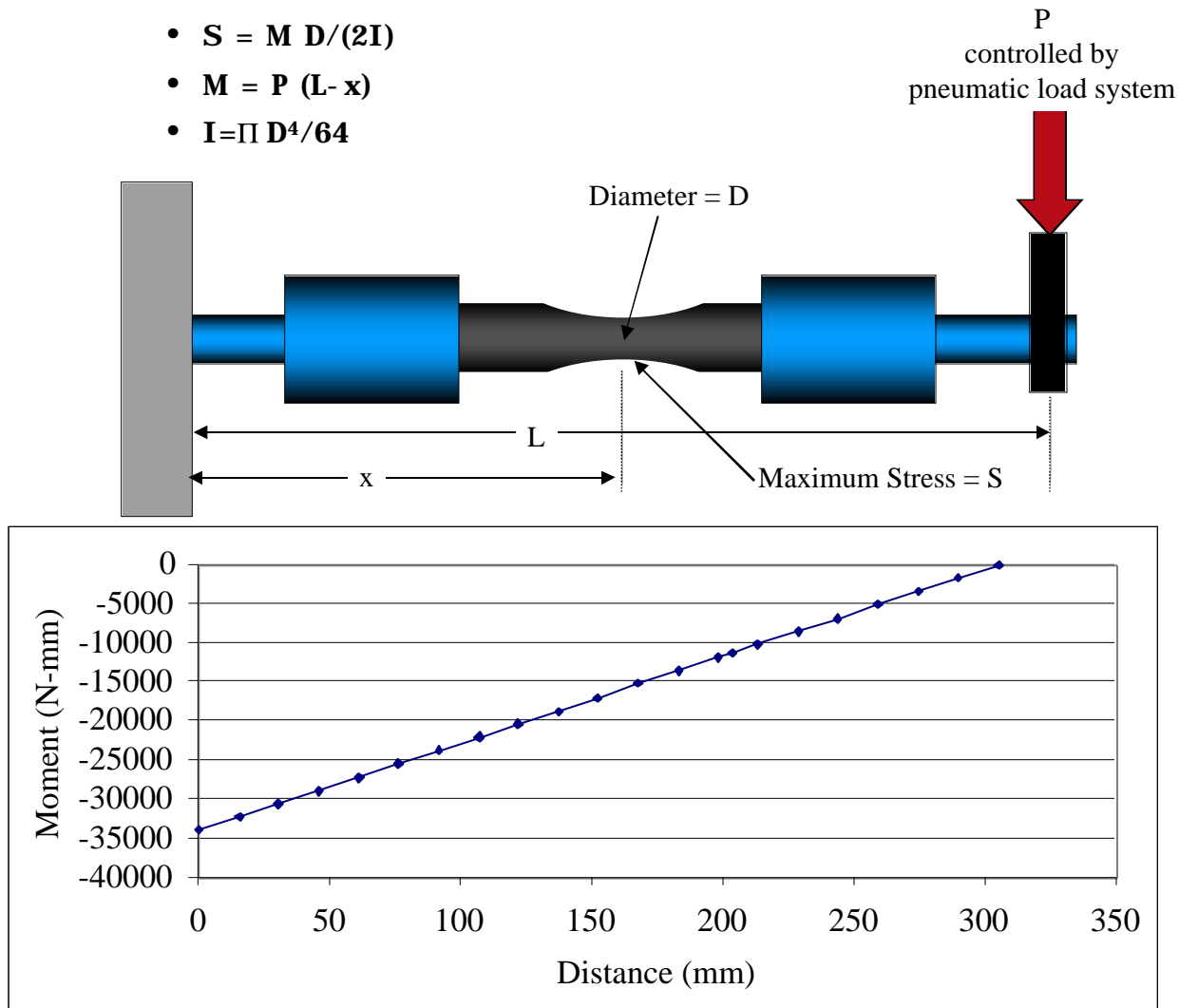


Figure 5: Schematic representation of the load geometry and corresponding moment diagram.

For the configuration in Figure 5, the maximum stress at the gage diameter is given by

$$S = M D / (2 I) \quad (12a)$$

$$M = P (L - x) \quad (12b)$$

$$I = D^4 / 64 \quad (12c)$$

where S is the stress, M is the bending moment, D is the gage diameter, P is the applied load, I is the moment of inertia, $L - x$ is the distance from the load point to the gage section. In order to verify the stresses predicted by Equations 12a-c, the strain was measured using a steel specimen having two diametrically opposed gages mounted in the gage section. Figure 6 compares the measured strain with that predicted from Equation 12a using an elastic modulus of 220 GPa. The fact the slope of the data is very close to 1 validates Equation 12.

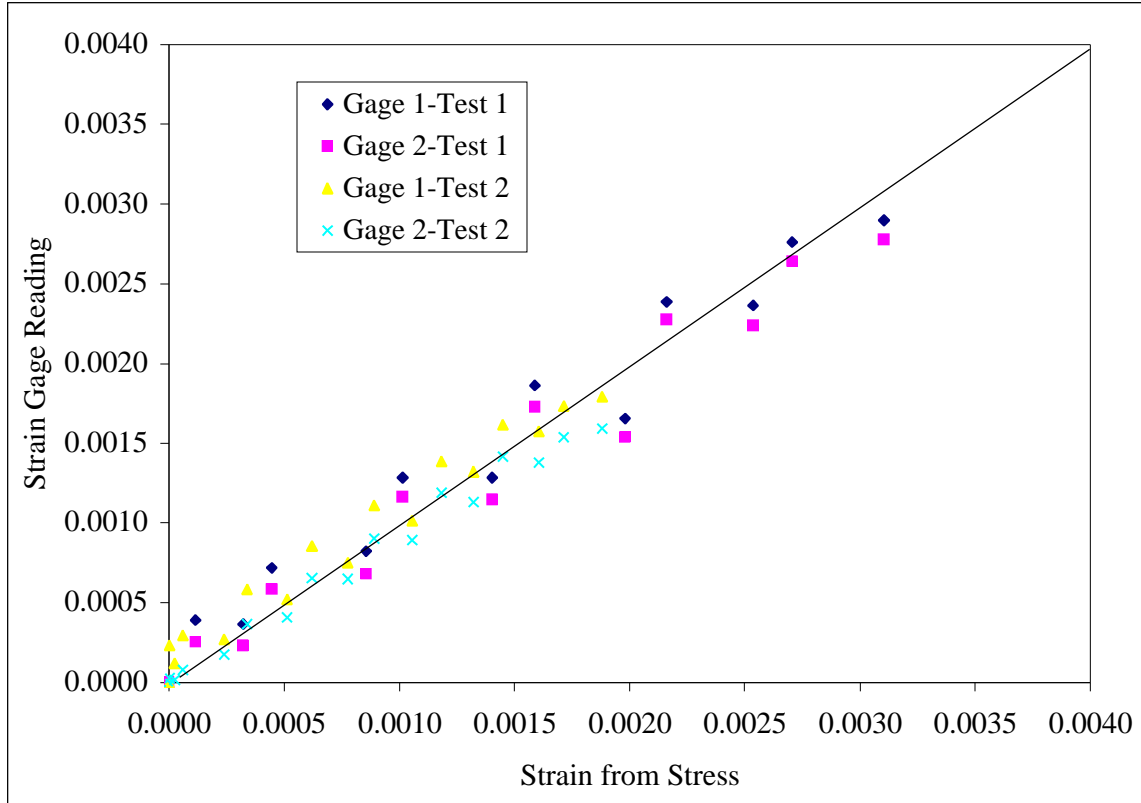


Figure 6: Comparison of measured strain with that predicted from Equation 12 for the experimental setup shown in Figures 4 and 5.

The RBF setup in Figures 4 and 5 was used to measure strength as a function temperature (700 and 850°C), stressing rate (0.0002 and 1.2 MPa/s), and rotational speed (0 and 1200 rpm). During slow loading rate tests, deformation of the left-hand grip¹ caused excessive deformation at the free end of the cantilever, which prevented the test from completing. This problem was attributed to the combined effects of high stresses² and temperatures in the left-hand grip, which caused the metal collets to creep. The application of several grip cooling and insulation schemes did not solve the problem. In an attempt to reduce the stresses in the vicinity of the left-hand grip, an opposing loading configuration was developed (Figure 7). For this load geometry, M is given by

$$M = (P_2 X_2 - P_1 X_1) - X (P_2 - P_1) \text{ (for } X < X_1) \quad (13)$$

where the Ps represent loads and the Xs are the distances from the fixed end (Figure 7). When $P_2 = P_1$, the moment for is independent of X as shown by the moment diagram in Figure 7. The stress is still given by Equation 12a. Subsequent strain measurements made with the gaged specimen were in good agreement with the strain values determined from the stress (Figure 8).

¹ This is the grip closest to fixed end of the cantilever.

² Note that the stresses in the left-hand grip are higher than those in the right-hand grip due to the higher bending moment.

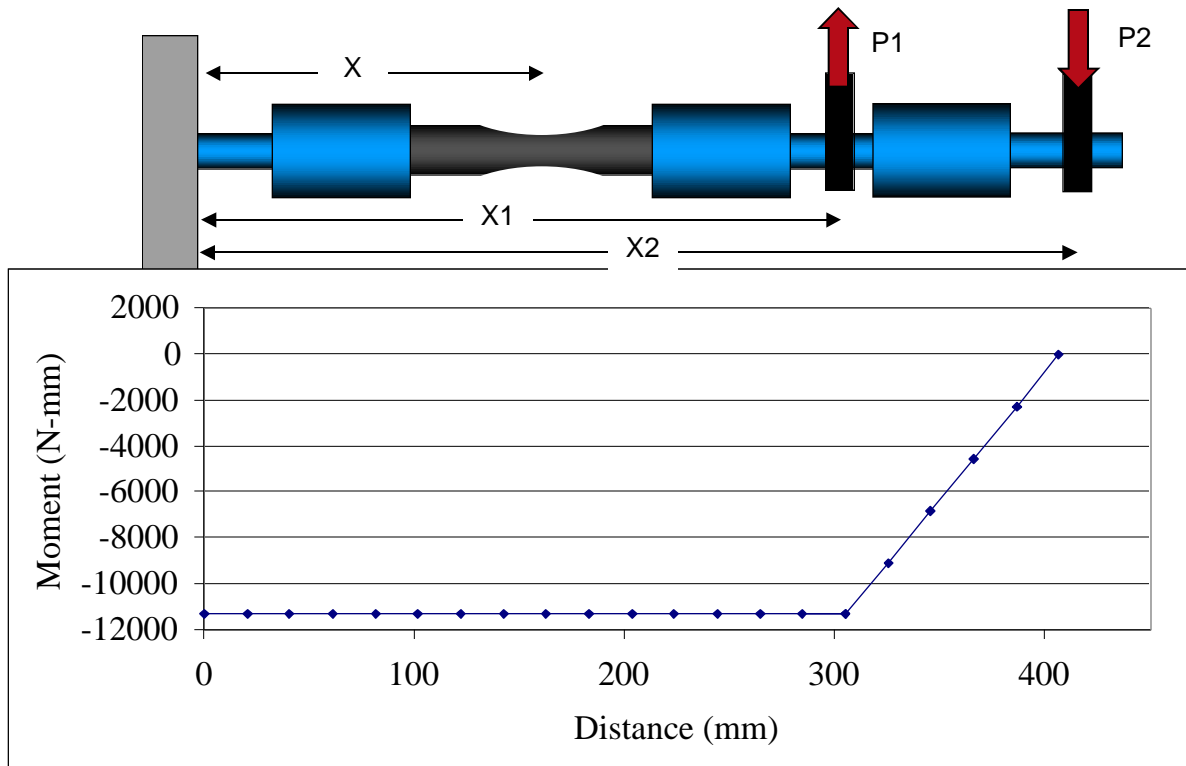


Figure 7: Schematic representation of the opposing load geometry and corresponding moment diagram.

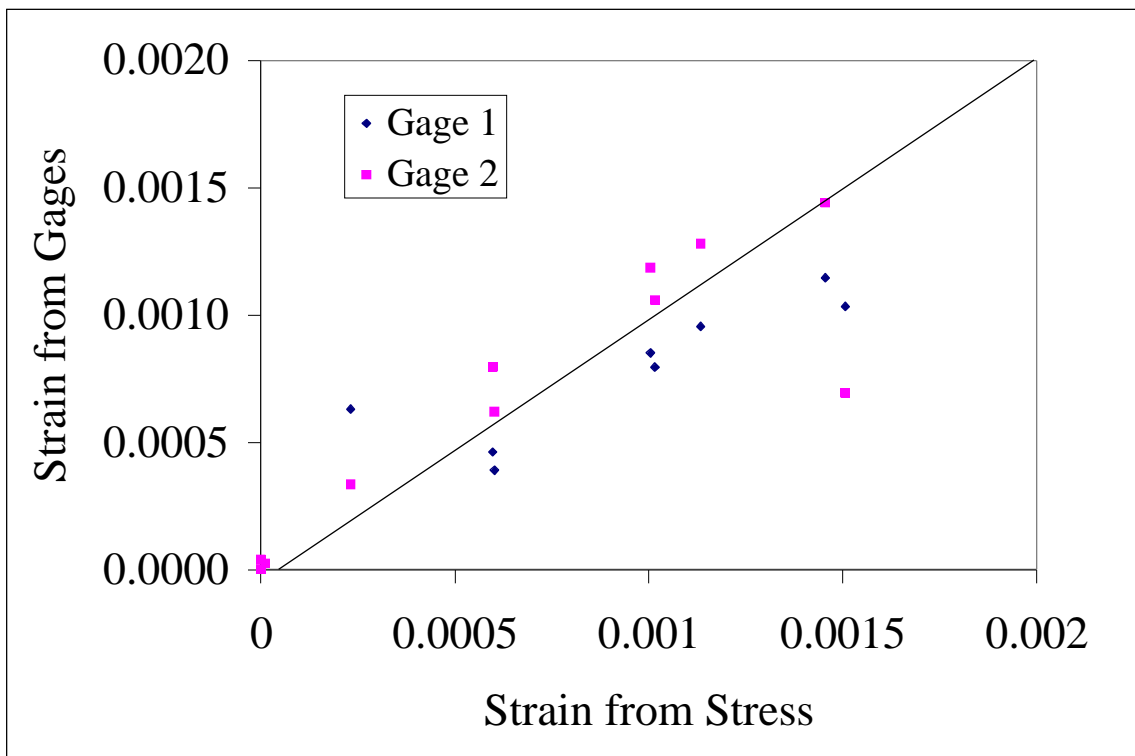


Figure 8: Comparison of measured strain with that predicted from Equations 1a and 2 for the experimental setup shown in Figure 7.

RESULTS AND DISCUSSION

Static Fatigue

The static fatigue data measured at 850°C using the GS44 flexure specimens are shown in Figure 9. As discussed in [2], the susceptibility of GS44 to time-dependent loss in strength was much greater at this temperature than that observed at temperatures <700°C. The associated strength degradation mechanism was attributed to softening of the intergranular phases, which ultimately led to viscous flow and separation of grain facets. Given sufficient time, this viscous flow was ultimately responsible for the formation of cavities within the intergranular phase. For example, Figure 10 compares the fracture surfaces of two dynamic fatigue specimens; one tested at 30 MPa/s and other at 0.003 MPa/s. At 0.003 MPa/s there was sufficient time for the cavitation to occur as evidenced by the skeletal pattern of the intergranular phase outlining the interfaces between adjacent grains. It should be noted that similar behavior was observed for a hot-isostatically pressed silicon nitride when tested under tensile loading at temperatures above 1200°C [3]. In that study, however, the temperatures were sufficiently high to activated addition deformation mechanisms including cavitation of the silicon nitride by a solution-precipitation process.

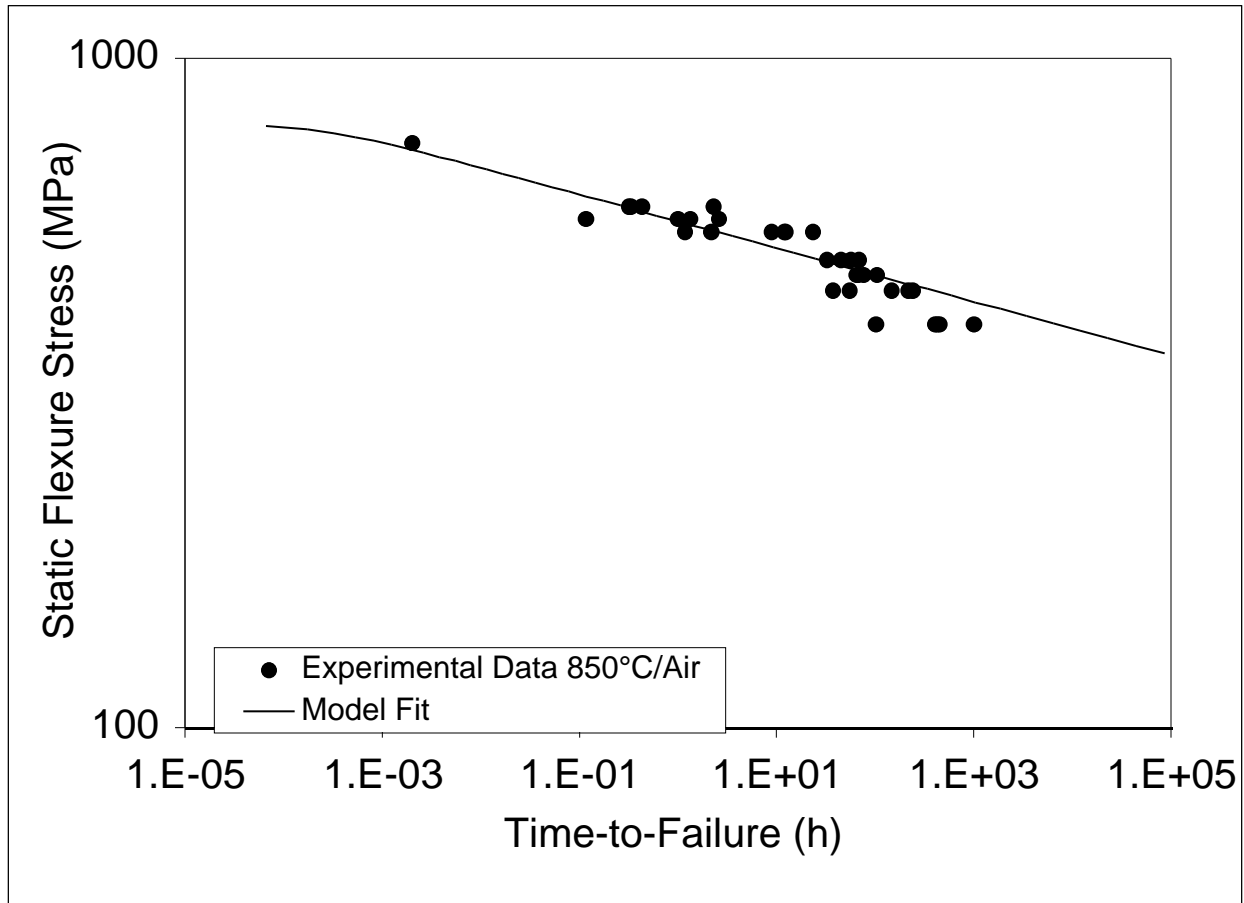


Figure 9: Flexural static fatigue data generated at 850°C. The symbols represent the experimental data while the solid line is the fit of these data to Equation 8.

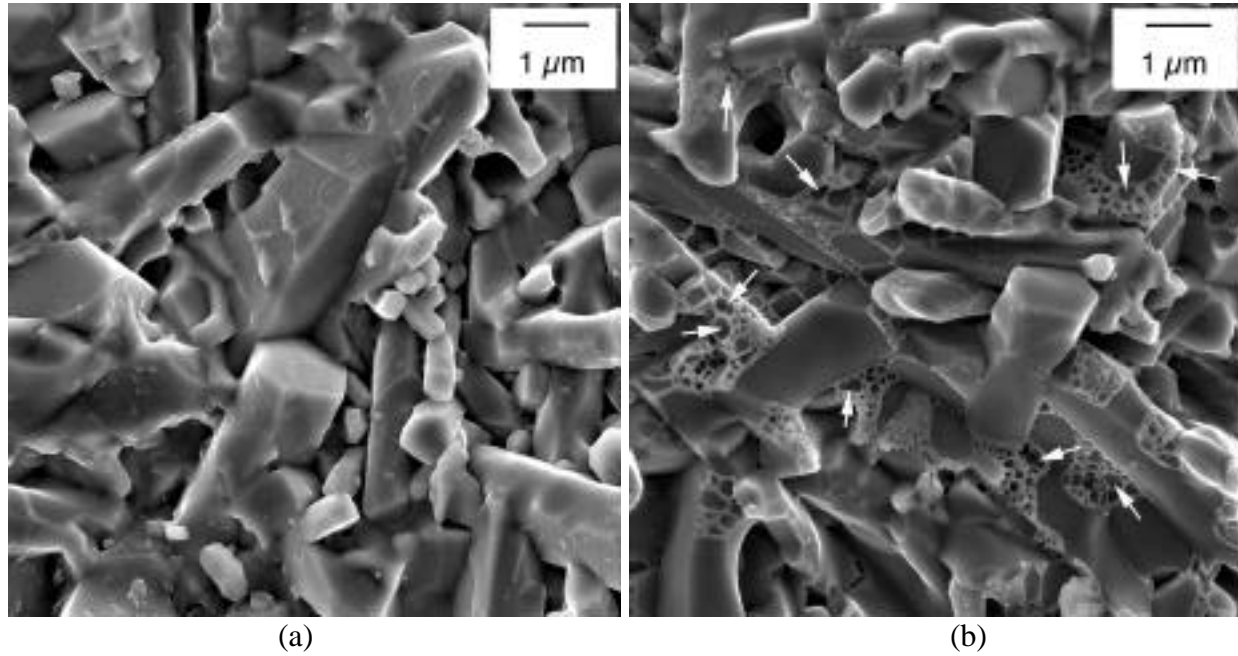


Figure 10: Comparison of fracture surfaces of two flexure specimens tested at (a) 30 MPa/s and (b) 0.003 MPa/s. The test temperature was 850°C.

The experimental static fatigue data were subsequently fit to Equation 8 by choosing values of S_i , N , and $V(K_{IC})$ which minimized the sum of the square of errors between predicted and measured lifetimes. The fracture toughness at 850°C was assumed to be comparable to the room-temperature value reported by the vendor ($8 \text{ MPa m}^{1/2}$). The resulting values of the crack growth parameters estimated using this iterative procedure are provided in Table 1. The solid line in Figure 9 illustrates the model prediction. Note that the value of $V(K_{IC})$ is relatively low. One might expect that it should be comparable to the speed of sound given that it associated catastrophic fracture. However, this parameter actually represents the velocity occurring at the intersection of the Region I slow crack growth curve with Region III curve as shown schematically in Figure 11. Because the Region III crack growth makes very little contribution to the time-dependent failure, it is treated as a vertical line in the development of the equations describing static, dynamic, and cyclic fatigue.³

Table 1: Crack growth parameters.

Parameter	Value	Comments
Y	1.5	Based on surface cracks
K_{IC} (MPa $\text{m}^{1/2}$)	8	Based on vendors information
$V(K_{IC})$ (m/s)	5×10^{-6}	
S_i (MPa)	800	
N	25	

³ The contribution of Region II slow crack growth to time-dependent failure is also ignored.

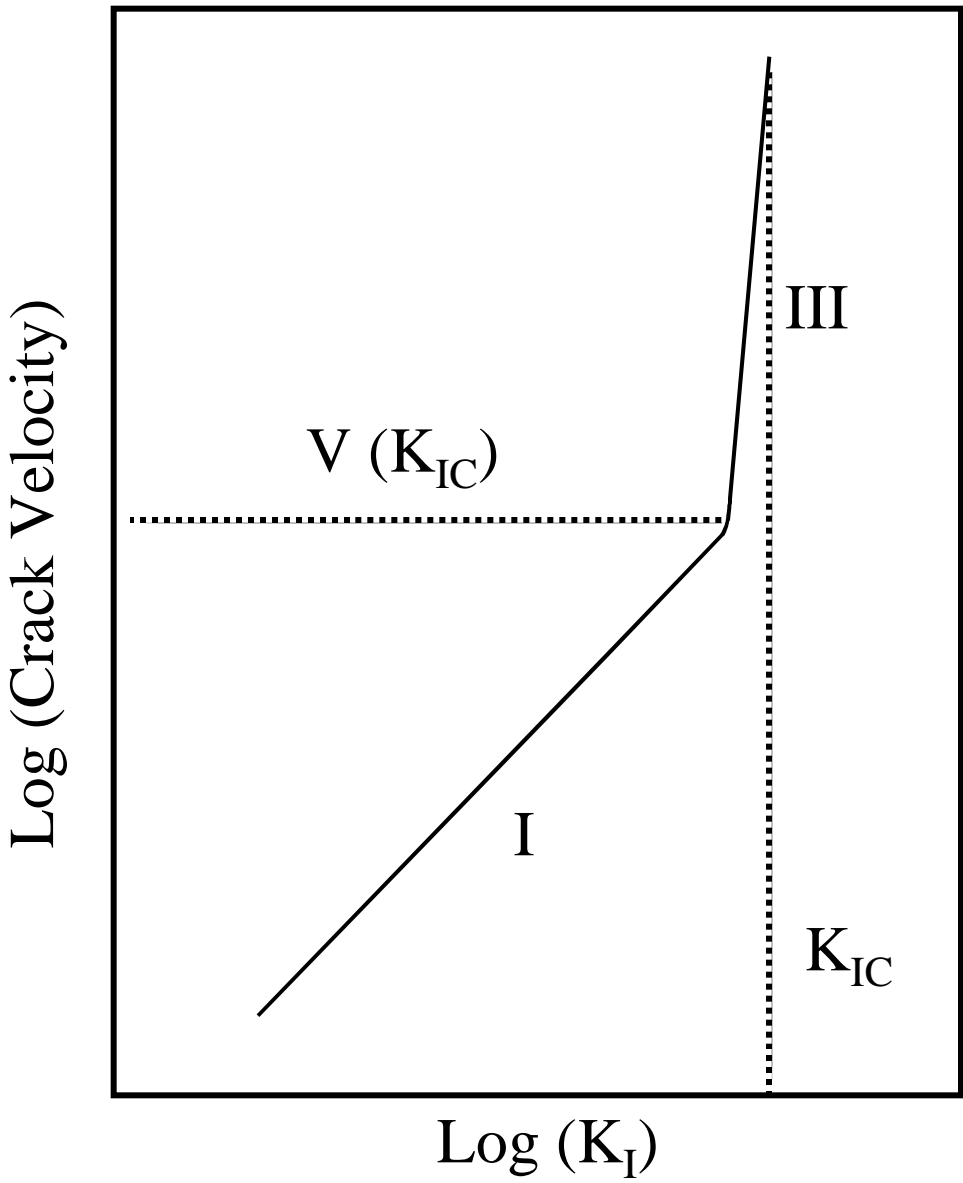


Figure 11: schematic representation of V-K_I behavior showing two regions of crack growth. Because the slope of Region III is very high, its contribution to time-dependent failure can be neglected. In this case, V (K_{IC}) represented the intersection of the Regions I and III curves.

Dynamic Fatigue

Figure 12 illustrates the results of the dynamic fatigue testing conducted at 850°C. The slow crack growth exponent, N, can be estimated from these data using the simplified form of Equation 9b:

$$(d/dt) = [(N-2)/(2(N+1))] V(K_{IC}) (Y S_i/K_{IC})^2 (S_i)^{-N} ()^{N+1}. \tag{14}$$

In this case $N+1$ is equal to the slope of strength-stressing rate plot. Using this method for the data in Figure 12, N was estimated as 33.

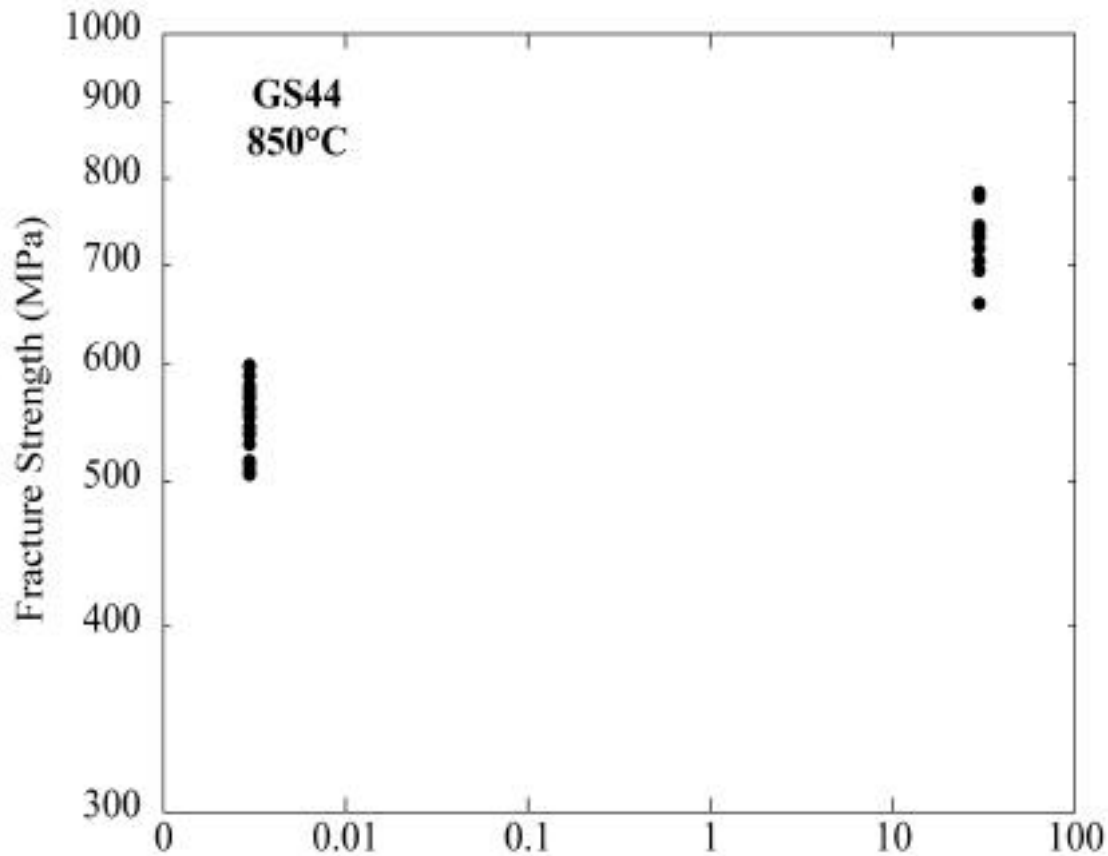


Figure 12: Strength versus stressing rate data for the GS44 material.

As indicated by the various forms of Equation 9, different combinations of strength, stressing rate, and time-to-failure (strength/stressing rate) can be used to describe the dynamic fatigue data. As shown in Figure 13, the use of strength versus time-to-failure facilitates the direct comparison of static and dynamic fatigue results. Note that the experimental dynamic fatigue data points are shifted to longer times due to fact that in a dynamic fatigue test the stress is not constant but increases linearly from zero to final fracture strength. The same relationship is reflected by the predicted static and dynamic fatigue curves. In the latter case the curve was predicted from the static fatigue results by applying the slow crack growth parameters in Table 1 to Equation 9c. The agreement is quite good.

It is clear in Figure 13 that Equations 8 and 9 predict a stress (strength) plateau as the time approaches zero. In this regime, the static and dynamic fatigue behaviors are controlled primarily by Region III crack growth (Figure 11), which is assumed to be very steep. Often the effect of Region III is ignored in the development of the slow crack growth equations which leads to simplified versions of Equations 8 and 9 in which $(S_f/S_i)^{N-2} \sim 0$. This can lead to significant errors in the prediction of the crack growth parameters particularly if much of the data are obtained at short times. This explains why the N value determined from the application of

Equation 14 to the dynamic fatigue data was significantly greater than that determined from the application of Equation 8 to the static fatigue data.

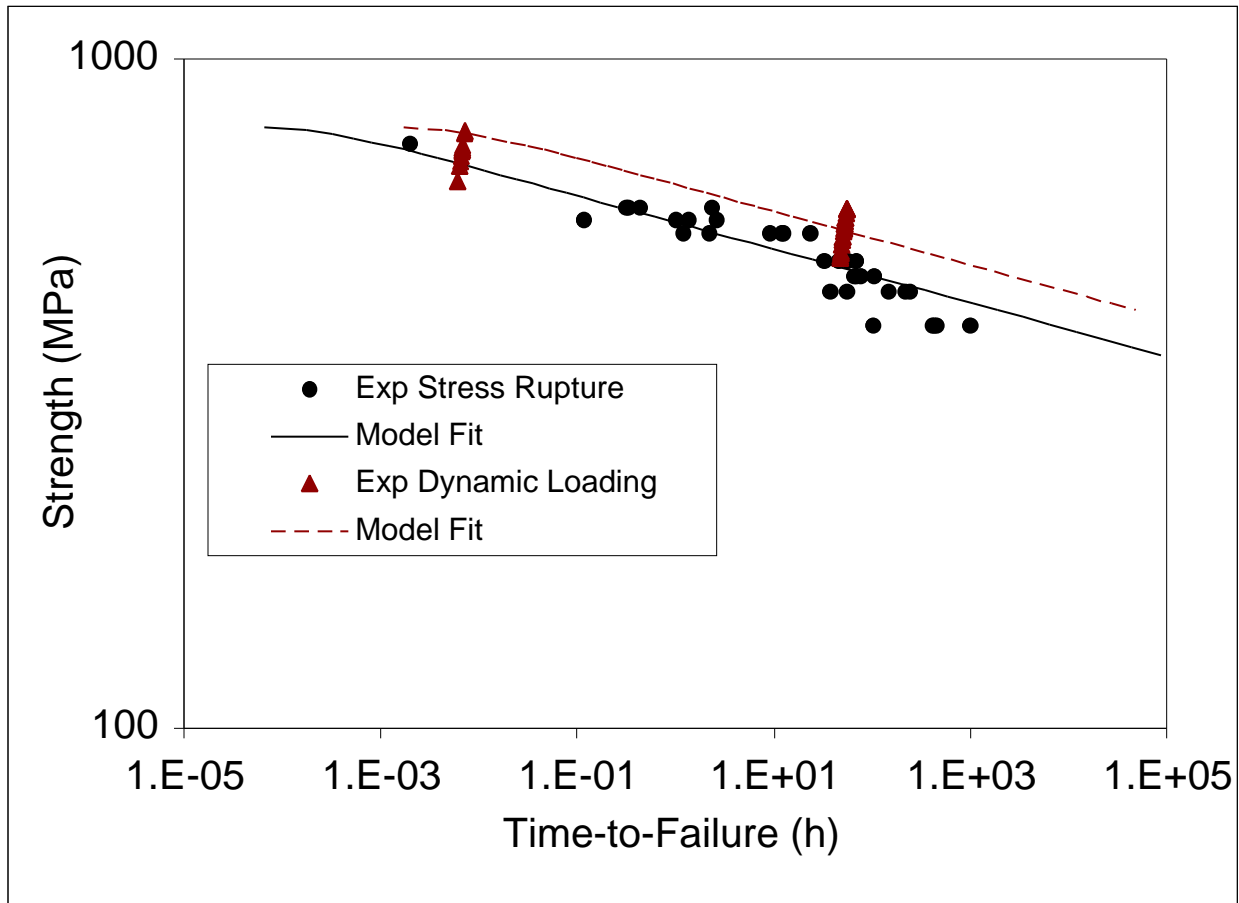


Figure 13: Comparison of static and dynamic fatigue results. The dynamic fatigue model fit was determined from the static fatigue results by applying the slow crack growth parameters in Table 1 to Equation 9c.

Cyclic Fatigue

The preliminary RBF tests were conducted using the single load point configuration (Figure 5) at two stressing rates with no rotation applied to the specimen. The purpose of these tests was to determine if the resulting strength versus stressing rate data were comparable to those obtained from the flexure specimens. Figure 14 compared the dynamic fatigue data obtained for the two specimen types. It is clear that at the slower loading rate, the RBF specimens did not exhibit the same drop in strength as did the flexure specimens. Therefore the RBF data failed to predict the slow crack growth behavior of the GS44 silicon nitride. This behavior was attributed to creep of collets located in the grip at the fixed end, which caused excessive movement of the free end of the specimen at the slower loading rate. This in turn led to eventual contact of the specimen free end with the furnace insulation, which effectively lowered the gage section stress.

Current effort is being placed on the deployment of the dual acting air cylinder system in Figure 7. This arrangement should lead to lower stresses in the grip located near the fixed end. Results of this testing will be reported in the final report for Subtask 11.

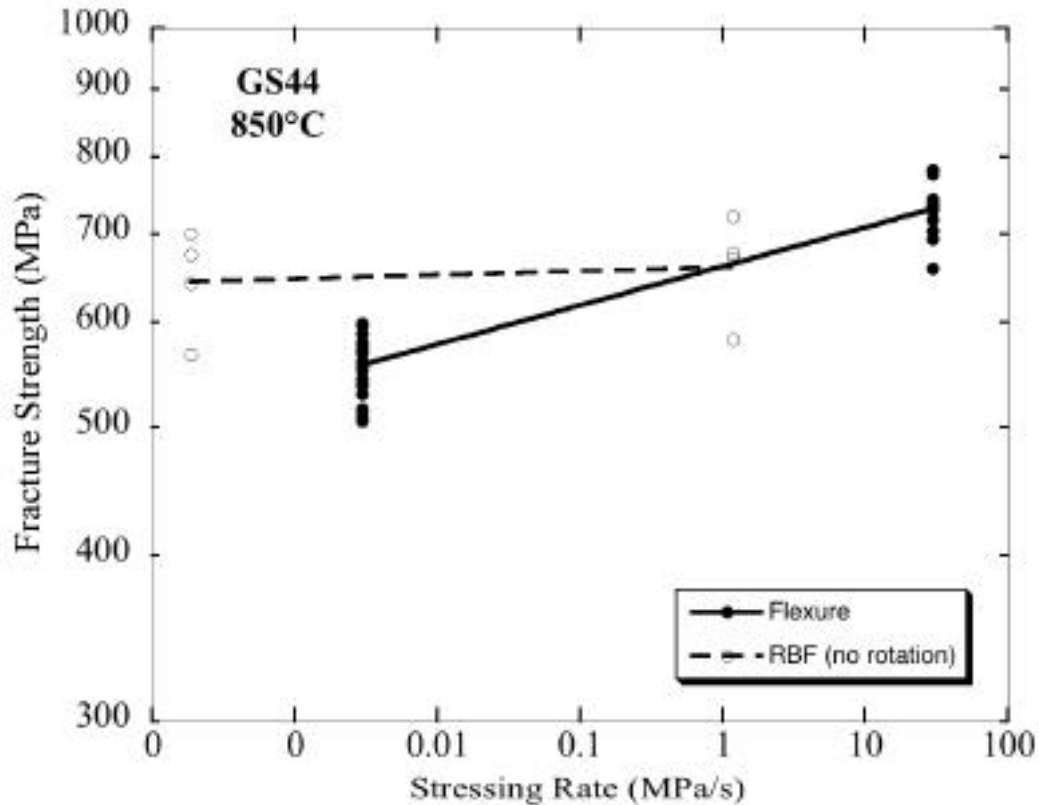


Figure 14: Comparison of dynamic fatigue results obtained from testing flexure and RBF specimens.

CONCLUSIONS

The GS44 silicon nitride was susceptible to slow crack growth at 850°C. This was reflected by the relative low value of the crack growth parameter, $N (= 25)$, estimated from the static fatigue of the flexure samples. The underlying mechanism was related to the softening of the intergranular phase, which resulted in extensive cavitation. The slow crack growth parameters

determined by fitting the experimental static fatigue data to Equation 8b were found to adequately predict the dynamic fatigue data obtained for the flexure bars.

Preliminary dynamic fatigue tests of the GS44 RBF specimens conducted at 850°C with no rotation exhibited no drop in strength with decreasing stressing rate. This result was attributed to excessive movement of the specimen, which was caused by creep of the grip collets at the slower loading rates. A new dual acting loading geometry is being used to eliminate with problem.

REFERENCES

- [1] M. K. Ferber, Kirchoff, G., Hollstein, T., Westerheide, R. Bast, U., Rettit, U., and Mizuno, M., "Thermal Shock Testing of Advanced Ceramics – Subtask 9 (Final Report)," Oak Ridge National Laboratory, Oak Ridge, Tennessee, Report No. MOO-107208, March 2000.
- [2] A. A. Wereszczak, H.-T. Lin, T. P. Kirkland, "Strength and dynamic fatigue of silicon nitride at intermediate temperatures," *J. Mater. Sci.* **37** 2669 – 2684, (2002).
- [3] M. K. Ferber and M. G. Jenkins, "Evaluation of the Strength and Creep-Fatigue Behavior of a HIPed Silicon Nitride," *J. Amer. Ceram. Soc.* , **75**, [9], 2453-62, 1992.